An integrated assay to probe endothelial glycocalyx-blood cell interactions under flow in mechanically and biochemically well-defined environments

Heather S. Davies,[1] Natalia S. Baranova,[2,‡] Nouha El Amri,[1] Liliane Coche-Guerente,[3] Claude Verdier,[1] Lionel Bureau,[1] Ralf P. Richter[2,4,*] and Delphine Débarre[1,*]

[1]Université Grenoble Alpes, CNRS, Laboratoire Interdisciplinaire de Physique (LIPhy), 38000 Grenoble, France. [2]Biosurface Lab, CIC biomaGUNE, Paseo Miramon 182, 20014 San Sebastian, Spain. [3]Université Grenoble Alpes, CNRS, Département de Chimie Moléculaire (DCM), Grenoble, France. [4]School of Biomedical Sciences, Faculty of Biological Sciences, School of Physics and Astronomy, Faculty of Mathematics and Physical Sciences, Astbury Centre for Structural Molecular Biology, University of Leeds, Leeds LS2 9JT, United Kingdom.

‡Current address: Institute of Science and Technology Austria (IST Austria), Am Campus 1, 3400 Klosterneuburg, Austria

*Corresponding authors: r.richter@leeds.ac.uk; delphine.debarre@univ-grenoble-alpes.fr

Abstract

Cell-cell and cell-glycocalyx interactions under flow are important for the behaviour of circulating cells in blood and lymphatic vessels. However, such interactions are not well understood due in part to a lack of tools to study them in defined environments. Here, we develop a versatile *in vitro* platform for the study of cell-glycocalyx interactions in well-defined physical and chemical settings under flow. Our approach is demonstrated with the interaction between hyaluronan (HA, a key component of the endothelial glycocalyx) and its cell receptor CD44. We generate HA brushes *in situ* within a microfluidic device, and demonstrate the tuning of their physical (thickness and softness) and chemical (density of CD44 binding sites) properties using characterisation with reflection interference contrast microscopy (RICM) and application of polymer theory. We highlight the interactions of HA brushes with CD44-displaying beads and cells under flow. Observations of CD44+ beads on a HA brush with RICM enabled the 3-dimensional trajectories to be generated, and revealed interactions in the form of stop and go phases with reduced rolling velocity and reduced distance between the bead and the HA brush, compared to uncoated beads. Combined RICM and bright-field microscopy of CD44+ AKR1 T-lymphocytes revealed complementary information about the dynamics of cell rolling and cell morphology, and highlighted the formation of tethers and slings, as they interacted with a HA brush under flow. This platform can readily incorporate more complex models of the glycocalyx, and should permit the study of how mechanical and biochemical factors are orchestrated to enable highly selective blood cell-vessel wall interactions under flow.

Keywords: Hyaluronan, CD44, glycocalyx, mechanics, biomimetics, cell-glycocalyx interactions

1. Introduction

The endothelial glycocalyx is a network of glycosaminoglycans (GAGs), adhesion proteins and glycoproteins that lines the luminal surface of the blood vessel wall. It acts as the gate-keeper of cell entry to the underlying endothelium by presenting a micron-thick [1], soft (10-1000 Pa) [2, 3], repulsive cushion to expel red blood cells, whilst displaying binding sites for immune cell and stem cell rolling, adhesion and transmigration.

Contributing to the selectivity of the endothelial glycocalyx is the linear polysaccharide hyaluronan (HA). HA is synthesised at the plasma membrane by HA synthase into polymers of several million Daltons, with repeating units of $\beta(1,4)$-*N*-acetyl-glucosamine and $\beta(1,3)$-glucuronic acid. Several microns long [4], HA polymers are thought to be anchored to the endothelium via HA synthases and HA receptors [5, 6], resulting in a thick HA coat protruding into the lumen as flexible loops and chains [7]. This gives rise to a HA backbone that provides a structural scaffold for the binding of other proteoglycans and proteins, forming a complex self-organised film that dynamically re-organises in response to external stimuli [8].

HA also provides binding sites for its cell receptor CD44: each polysaccharide chain possesses hundreds of binding sites, although a fraction of these may be masked by other HA binding proteins. HA-CD44 interactions have been shown to be necessary for the capture and

rolling of subsets of CD44+ T-lymphocytes [9], and the firm adhesion of CD44+ neutrophils on the blood vessel endothelium [10, 11] in response to inflammatory stimuli *in vivo*. In addition to leukocytes [9, 12-14], stem cells [15-17] and cancer cells [16, 18, 19] employ HA-CD44 binding for cell adhesion, as demonstrated by *in vitro* assays utilising CD44+ cells and soluble HA or immobilised HA/HA-expressing endothelial monolayers under static conditions or inside flow channels, which mimic the physiological shear stress of post-capillary venules (~1-4 dyn/cm^2 [20]). Such flow assays have also revealed that HA-CD44-mediated adhesion is tightly regulated, by mechanisms including CD44 remodelling [21] under activating conditions [13, 22, 23], and changes to HA architecture in response to inflammatory effectors [5, 23-26].

The wealth of information derived from *in vitro* flow assays has highlighted their biochemical relevance. In addition to biochemical factors, there is now ample evidence that substrate mechanical properties, such as stiffness and thickness, also profoundly influence cell adhesion and signalling [27, 28]. However, as with other cell-glycocalyx interactions studied with *in vitro* model platforms, the surfaces utilised are unlikely to reproduce key physical properties of the glycocalyx. This is due in part to the utilisation of immobilisation strategies in which the orientation and surface density of glycocalyx molecules are not well controlled, resulting in films of unknown softness and thickness. As such, physical factors have been almost completely overlooked in flow assays, and their influence on cell-glycocalyx interactions under flow remains largely unknown.

Another factor that has hindered the incorporation of glycocalyx physical parameters into flow assays is the lack of tools to characterise them. Conventional flow assays have employed imaging modalities, such as bright-field microscopy, to shed light on immune cell capture, firm adhesion and rolling velocity under flow by observation of displacement along the surface (in *x*- and *y*-directions) [9, 13, 15, 16, 18, 21]. However, bright-field microscopy is largely insensitive to displacements perpendicular to the surface (in *z*-direction) and so cannot differentiate: (i) the inherent thickness of the model surfaces; or (ii) the position of interacting cells with respect to thick glycocalyx-mimetics.

A label-free optical technique that offers sensitivity to *z*-directionality is reflection
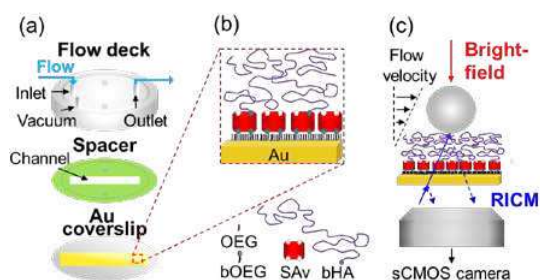

Fig. 1: Schematic depiction of the flow assay. (a) The parallel-plate flow chamber provides laminar flow at tuneable rates and incorporation of coverslips for functionalisation, such as gold-coated coverslips here. (b) HA brushes generated *in situ* on top of a SAv-monolayer on a gold surface modified with covalently attached biotin groups (bOEG/OEG monolayer). (c) Mounting of the assembled flow chamber on a multi-modal inverted microscope with RICM capability provides a method to examine bead height with respect to HA films, in addition to velocity under flow.

interference contrast microscopy (RICM). Based on interferences in reflected light, RICM can distinguish the distance between an object and a surface, providing a method to characterise the thickness of a surface layer with nanometer precision. Furthermore, the sensitivity of RICM in flow assays has been highlighted by the detection of additional arrests of particles interacting with a surface by observation of particle height with respect to the surface, compared to measurement of velocity alone [29]. Thus, it is an ideal tool to study interactions between thick glycocalyx-mimetics and cells/cell-mimetics under flow.

Here, we develop an *in vitro* flow assay to study the behaviours of circulating cells/cell-mimetics on well-defined glycocalyx mimetics, with controllable chemical and physical parameters. To this end, we integrate versatile surface chemistry and RICM (along with bright-field microscopy) with a microfluidic device. We describe the tools necessary for the implementation of this methodology into a conventional inverted optical microscopy setup and illustrate the capabilities of our platform by probing HA-CD44-mediated cell-glycocalyx interactions. Specifically, we demonstrate the formation of tuneable HA based glycocalyx-mimetics, including those of physiological thickness and softness, and their characterisation *in situ* within flow channels. In depth characterisation of the physical parameters of such films is described here with reference to polymer physics and soft matter theory. We have
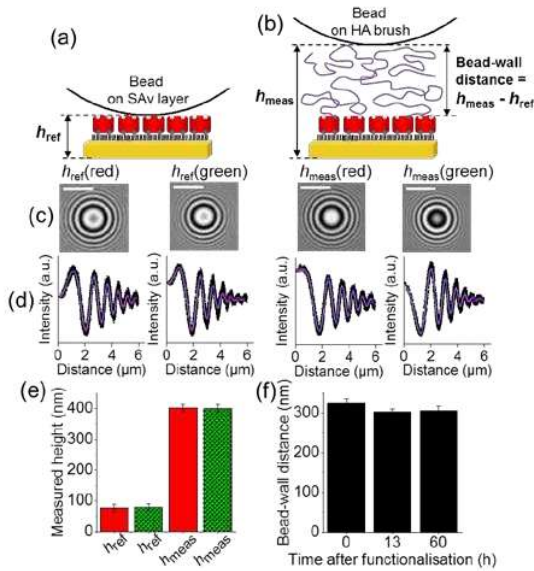
Fig. 2: Characterisation of HA brush height with RICM using 25 µm uncoated microbeads. (a, b) Schematic representation of beads on a SAv monolayer and HA840-brush, respectively. (c) RICM images appear as fringe patterns and were taken at two wavelengths (red and green) on SAv (h_{ref}) and HA (h_{meas}). Scale bar is 5 µm. (d) Intensity profiles as a function of the distance to the pattern centre of RICM fringe patterns (black), average data (magenta) and the fitted model (blue). (e) Measured heights (raw data) on SAv (h_{ref}) and HA840 (h_{meas}) from RICM images captured in red and green wavelengths ($n \geq 24$). The h_{ref} and h_{meas} include contributions from the optical properties of the gold (see Supplementary Information), but their difference (= h_{meas} - h_{ref}) provides a physical thickness termed here bead-wall distance, a measure of HA film thickness. (f) Bead-wall distance measured over the typical length of time of an experiment ($n \geq 25$).

deliberately focused the main text on the principles of the setup and data analysis and provide technical details and mathematical derivations as Supplementary Information for the interested reader. In addition, we provide selected experimental examples of the insight that can be derived with this platform by demonstrating the 3D trajectories of CD44+ cell-mimetics on a HA film, and the dynamic behaviours of living CD44+ AKR1 T-lymphocytes as they roll on a HA brush under flow. With simple adaptation, this platform should incorporate alternative or more complex glycocalyx-mimetics for the further study of cell-glycocalyx interactions in well-defined biochemical and mechanical environments under flow.

2. Results and discussion

In Section (2.1) we present the details of brush formation and characterisation using RICM and polymer theory, with the aim to provide a comprehensive guide to implement our methodology. Subsequently, in Section 2.2, we highlight key applications of this platform demonstrated with selected HA brushes. The reader can refer to these somewhat independent sections as desired, in order to discover brush formation/characterisation and interaction studies with CD44+ cells/cell mimetic, respectively.

2.1. Formation of HA brushes with controllable thickness, softness and binding site density

2.1.1. In situ formation of HA films within a flow chamber

Brushes of one-end grafted HA were generated *in situ* within a parallel-plate flow chamber using biotinylated polymeric and oligomeric HA samples of well-defined molecular weight (M_W), based on functionalisation protocols established previously [30, 31]. The parallel-plate flow chamber, held together under vacuum, consisted of an upper deck (with inlet and outlet for controllable flow), a spacer with defined channel dimensions and a coverslip displaying on its surface a layer of biotins covalently attached via short oligo (ethylene glycol) linkers to a transparent gold film (Fig. 1a-b). Injection of streptavidin (SAv) *in situ* created a monolayer of binding pockets for the further immobilisation of biotinylated HA (bHA) to generate HA brushes (Fig. 1b). More generally, this SAv platform can be used as a 'molecular printboard' to create other cell surface/glycocalyx-mimetic films from a single or a mixture of biotinylated molecules (as demonstrated previously [30, 32]). Furthermore, the setup is compatible with the use of other types of functionalised surfaces (e.g., thiols on gold and silanes on glass). As such, this enables the preparation of bespoke glycocalyx and cell surface models of desired composition and complexity.

2.1.2. Characterisation of HA brush height by RICM

The assembled flow chamber was mounted on a microscope with RICM capability (Fig. 1c and Supplementary Information Section 1.1). RICM is an optical technique sensitive to the distance of objects up to a few µm from a surface [33], providing a unique way to examine objects, such

as cells or beads, as they interact with a surface. For symmetrical objects, such as microbeads, the distance between a bead and surface (bead-substrate distance) can be determined quantitatively. This was performed here for precise (to within ~10 nm) characterisation of the thickness of HA brushes.

Microbeads were injected into the flow chamber and allowed to settle on the bottom surface before and after addition of bHA, thus resting either on top of the SAv monolayer or HA brush, respectively (Fig. 2a-b). Images of beads were captured in RICM, in which reflection from the surface of the bead closest to the substrate generates a fringe pattern (Fig. 2c). Capture of images in two wavelengths of light (red (635 nm) and green (534 nm)) enabled precise quantification of height (Supplementary Information Section S1.2). Visual comparison clearly illustrates that the fringe patterns on the SAv surface and a HA brush composed of polymeric HA of M_W = 840 kDa (HA840) appear different, reflecting the different heights of the beads with respect to the gold substrate.

Quantification of the bead-substrate distance was performed to ascertain the thickness of the HA brush. To this end, intensity profiles were generated from the captured fringe patterns and fitted with a function that accounts for the optical properties and the geometry of the system (Fig. 2d, Supplementary Information Section 1.2). Subtraction of the reference bead height measured on the SAv layer (h_{ref}) from that measured on the HA brush (h_{meas}), followed by averaging of values obtained in red and green wavelengths was performed to obtain the thickness of the HA brush at rest (bead-wall distance; Fig. 2e-f).

The HA brushes generated were stable and homogeneous. Following a slight reduction in HA brush thickness of ~5 % (Fig. 2f, t = 13 h) during overnight equilibration, likely due to loss of either weakly bound bHA or SAv bound monovalently rather than multivalently to the surface [34], surfaces showed stable thickness with no significant change over the course of several days (Fig. 2f, t = 60 h). Thus, all subsequent experiments were performed following an overnight equilibration step, and could take place for several days. In addition, HA brushes showed high homogeneity, as demonstrated by the relatively low standard deviation of the mean film thickness across measurements made throughout the flow channel length (Fig. 2e-f, error bars). We also ascertained
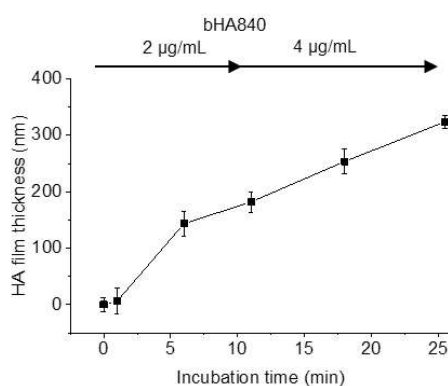

Fig. 3: Tuning the density and thickness of a HA840 brush. HA brush thickness changes with incubation time and concentration of bHA, measured *in situ* with RICM. All measurements were performed on a single surface. Error bars represent standard deviations ($n \geq$ 20 beads).

that gravitational forces on the beads do not affect the determination of HA brush thickness, and that photo-damage of the brush by the illuminating light is negligible over the course of an assay under the conditions used here (Supplementary Information Section 1.3).

2.1.3. Tuning HA brush thickness

Tuning of the thickness of HA brushes was achieved by controlling the incubation conditions of bHA during functionalisation. Small biotinylated molecules can saturate all free binding pockets on the SAv monolayer, which defines a maximal coverage corresponding to a root-mean-square (rms) distance of around 5 nm [34]. Larger biotinylated species, such a polymeric bHA, however, cannot access all sites due to steric hindrance imposed by bulky anchored bHA chains on the surface. Thus, at low enough surface coverages polymeric bHA adopts an unrestricted 'mushroom' conformation in which individual HA chains adopt the shape of a random coil and do not perturb one another on the surface. At higher coverages, however, denser packing causes repulsion of neighbouring bHA polymers, and their stretching away from the surface ('brush' conformation), resulting in increased HA film thickness. As demonstrated for HA840 in Fig. 3, adjustment of incubation time and/or bHA concentration, in combination with *in situ* RICM characterisation, provided a simple and precise method to tune the brush to a desired thickness. Here, in order to demonstrate the structurally diverse HA brushes that can be generated with our methodology, we chose incubation conditions to yield HA840-low density (HA840-l) and high-density (HA840-h)
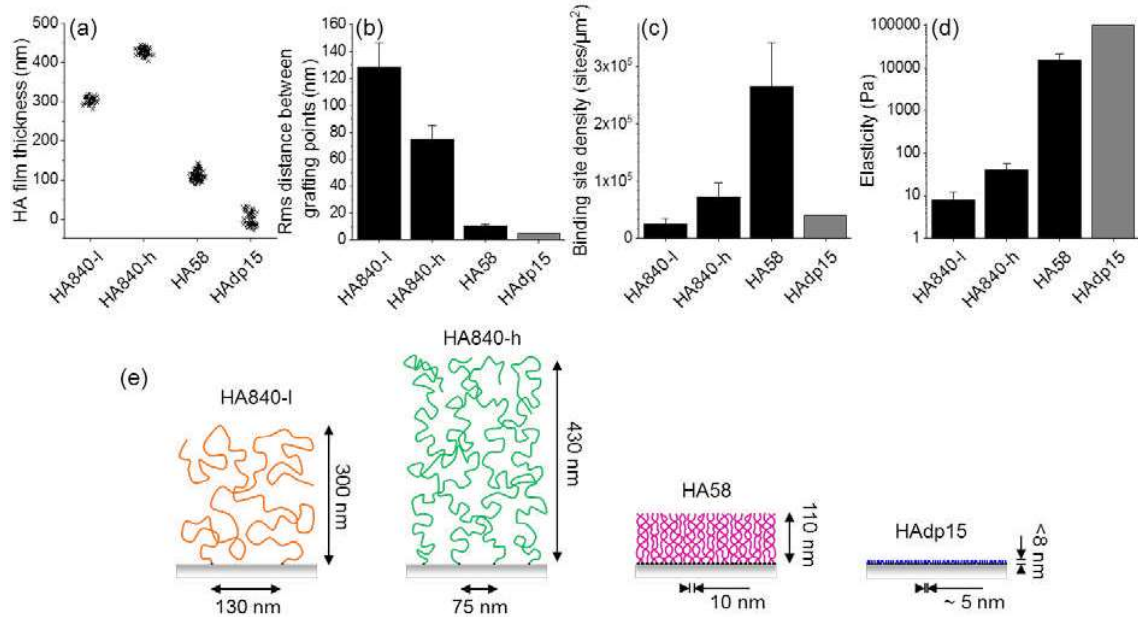
Fig. 4: Generation of HA brushes with tuneable thickness, softness and density of CD44 binding sites. (a) HA film thickness measured by RICM on various surfaces. Each point represents the bead-wall distance of a single microbead, with multiple microbeads ($n \geq 46$) measured along the length of the flow channel. Thickness measurements of HA polymer brushes HA840 and HA58 were used to determine (b) the root-mean-square (rms) distance between HA grafting points, (c) the surface density of CD44 binding sites, and (d) the brush elasticity (longitudinal modulus). Measured thicknesses and data derived from those measurements are shown in black. For HAdp15, rms distance, elasticity and surface density were estimated and are shown in grey. Error bars show relative standard error of the mean. (e) Schematic representation of the various HA films generated, their measured thickness and calculated rms distance between grafting points (not drawn to scale).

brushes, with brush thicknesses of 300 ± 10 nm and 430 ± 9 nm (mean ± standard deviation), respectively (Fig. 4a).

To produce more substantial differences in thickness, functionalisation with distinct bHA species of well-defined M_W was very effective. A shorter polymer of M_W = 58 kDa and oligomeric HA of 15 monosaccharides were used to form HA58 and HAdp15 films, respectively. Incubation conditions were chosen such that a measured thickness of 110 ± 12 nm was achieved for the HA58 brush (Fig. 4a). HAdp15 was incubated under saturating conditions, to give rise to a thin, densely packed film [31]. As shown in Fig. 4a, the height of the HAdp15 could not be differentiated from that of the underlying SAv layer using RICM. This reflects the short contour length of HAdp15 (7.5 nm), which thus produces a HA layer of <8 nm.

The determination of thickness of polymer HA brushes provides a powerful strategy to extract other key parameters about brush physical and chemical properties. For instance, application of polymer physics theory enables the distance between grafted HA chains to be determined [35], and from this both the

density of CD44 binding sites and the elasticity of the brush can be estimated, as described in the following sections.

2.1.4. Estimation of HA surface density

From the measured brush thickness H_o, the rms distance between individual polymer chains, ξ, was estimated from:

$$\xi^2 = \frac{8}{\pi^2} \frac{pv}{b} \left(\frac{l_c}{H_0}\right)^3 \qquad \text{Eq. (1)}$$

with b the monomer unit length (b = 1 nm, considering the basic HA disaccharide unit as the monomer) and l_c the polymer contour length calculated as $b \times$ (polymer M_W)/(monomer M_W). The intrinsic chain stiffness p = 13.9 (a measure for the bending rigidity), and the monomer effective excluded volume v = 3.67 nm^3 (a measure for the monomer size and also the inter-chain repulsion) were previously determined in an earlier study of HA brushes [35]. In this way, the values of ξ were calculated as 130 ± 18 (HA840-l), 75 ± 10 (HA840-h) and 10.4 ± 1.2 nm (HA58, Fig. 4b). For oligomeric HAdp15, the rms distance was estimated as 5 nm assuming it saturates the binding pockets on the SAv monolayer [31, 34].

5

2.1.5. Estimation of CD44 binding site density

The density of binding sites for CD44 within the HA brush, Γ_{bs}, was estimated as:

$$\Gamma_{bs} = \frac{M_p}{M_{bs}} \xi^{-2} \qquad \text{Eq. (2)}$$

where M_p and M_{bs} are the molecular weights of the polymer and the CD44 binding site (taken here as 5 disaccharide units, based on previous reports [6, 36, 37]), respectively. Therefore, in Eq (2) M_p/M_{bs} provides the number of CD44 binding sites per HA chain, and ξ^2 accounts for the number of HA chains per surface area. The HA polymer brushes generated here display CD44 binding site densities ranging from ~27 × 10³ sites/µm⁻² for HA840-l to 280 × 10³ sites/µm⁻² for HA58 (Fig. 4c). For HAdp15, 40 × 10³ sites/µm⁻² was estimated from the rms distance of 5 nm and 1 binding site per chain. These values reflect the total density of binding sites on the surfaces, which for polymeric HA brushes comprises sites that are present along the entire polymer length, including those closest to the wall, which may not be easily accessible.

2.1.6. Estimation of HA brush stiffness

The surface density of HA chains also provides the means to ascertain brush stiffness. Computation of the brush elastic (longitudinal) modulus, M, a measure of brush stiffness, was performed using the following equation (see Supplementary Information Sections S1.4-1.6 for derivation and validation):

$$M \approx \frac{13kT}{\pi \xi^3} \qquad \text{Eq. (3)}$$

where kT is the thermal energy. As shown in Fig. 4d, the elastic moduli calculated for the HA-polymer brushes were 8 ± 4 Pa (HA840-l), 40 ± 18 Pa (HA840-h) and 15.3 ± 6.2 kPa (HA58). For comparison, a 0.4 % agarose gel has an elasticity of ~1 kPa [38]. Thus, the brushes are very soft, particularly those composed of the long HA840 polymer. Since HAdp15 does not behave as a polymer, and is organised as a very thin film, its stiffness is likely to be dominated by the underlying substrate and thus in excess of 100's kPa.

We note that for less well-defined, or more structurally complex films, such as brushes composed of HA chains of high polydispersity, or films incorporating additional molecules of the glycocalyx or cross-links, the above-described method to estimate brush stiffness cannot be used. Two alternative methods that are applicable for these films are described in Supplementary Information Sections S1.5-1.6. One is based on the film indentation at rest by the gravitational force of beads of varying size. The other is based on a phenomenon called elastohydrodynamic lift – the lift of non-interacting beads on soft films under flow – which we recently reported [39].

Taken together, by controlling polymer length and grafting density, this section has demonstrated how HA films can be custom-made to have desired physical (thickness, softness) and biochemical (density of binding sites) parameters using our methodology. The brushes generated here show examples ranging from thick and very soft, to thin and rigid (Fig. 4e). Furthermore, the range of accessible brush heights and elastic moduli covers the mechanical properties of the endothelial glycocalyx (which may vary, e.g., upon inflammation, a phenomenon that remains to be studied) [1-3]. Thus, they are potent models for the examination of blood cell-glycocalyx interactions under a range of physiologically relevant well-defined environments. To further demonstrate the capabilities of our platform, we provide in the next section selected experimental examples of the insights that can be obtained for interacting regimes using CD44+ cell mimetics and living cells on selected HA films.

2.2. Probing the interactions of CD44+ cells and cell-mimetics with HA films under flow

2.2.1. Development of well-defined cell-mimetics

In addition to non-interacting microbeads described until now, the platform developed here can incorporate interacting cell-mimetics (e.g., functionalised microbeads) and living cells. Functionalised microbeads reduce the complexity of the system by confining the shape of the circulating cell to a simple sphere. Their receptor presentation can be tuned whilst maintaining cell size. To illustrate this, we used commercially available 15 µm polystyrene beads coated with SuperAvidin (SuAv, a modified form of SAv with reduced background binding) with a defined density of biotin binding sites. Here, a CD44 ectodomain construct with a biotin at the C-terminal end (bCD44) was incubated with SuAv beads to yield CD44+ beads, where the location of the biotin ascertains that the receptor orientation on the bead is comparable to the cell surface. Coverage was easily tuned by controlling the incubation concentration of bCD44, and the receptor surface density was determined by flow cytometry (Fig. 5; see Supplementary Information Section S1.7 for details).
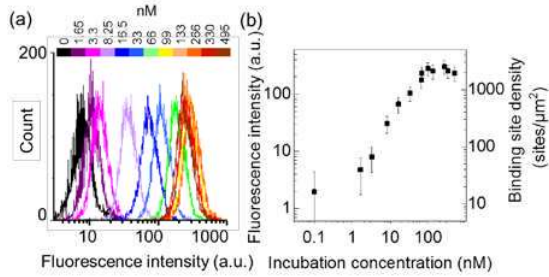
Fig. 5: Characterisation of CD44+ beads. (a) Flow cytometry of CD44-coated beads, after staining with the anti-CD44 antibody IM7-FITC. (b) Median fluorescence (left axis) and CD44 surface density (right axis) from flow cytometry data in (a). Error bars represent robust standard deviations of the median (see Methods Section 4.2.1).

The beads functionalised here covered a range of densities from ~20 to 3000 CD44 molecules per μm^2, equivalent to $10^4 – 10^6$ molecules per bead. This is comparable in order of magnitude to the number of CD44 receptors reported on monocytes [40], cancer cell lines [41] and macrophages [42].

2.2.2. Examining the interactions of CD44+ cell-mimetics on a HA film in 3D: stops and go's under shear stress

Specific interactions between CD44-HA could be probed, as demonstrated here for CD44+ beads (saturated coverage) on a HAdp15 film. Videos of beads were recorded using RICM at 100 frames per second (fps) under fixed flow rates (converted to shear stress, see Methods Section 4.2.6). Tracking procedures were developed in order to generate trajectories of beads as they moved over the HA surface (as described in the Supplementary Information Section S1.8) . This determined instantaneous bead velocity from x- and y- positions, while RICM fringe patterns were fitted to obtain bead-wall distance. In this way 3D trajectories of single beads were generated with high throughput. The tracking precision is highlighted by the estimated lateral resolution of RICM for the beads used in this experiment of ~ 5.5 ± 1.0 nm (Supplementary Information Section S1.9).

As shown in Fig. 6a, the 3D trajectory of a single CD44- (SuAv) bead at low shear (0.16 dyn/cm^2) showed relatively constant velocity of ~60 µm/s (closed black squares), and a bead-wall distance of ~70 nm (open black circles). This higher bead-wall distance for SuAv beads than uncoated beads on HAdp15 (Fig. 4) could suggest a higher surface roughness on the SuAv coated beads. In comparison, the 3D trajectory of
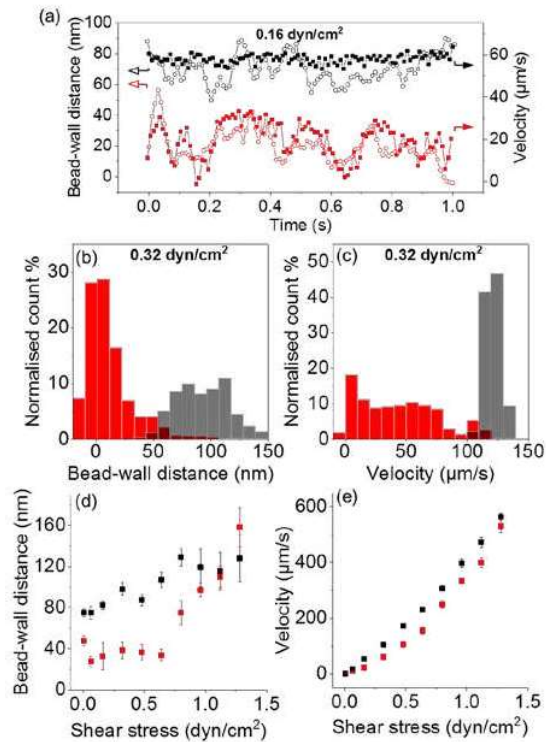

Fig. 6: Interactions of CD44+/- beads on a HAdp15 film. (a) Individual 3D trajectories of a CD44- (black) and CD44+ (red) bead, showing bead-wall distance (open circles) and instantaneous velocity (closed circles), recorded at 100 fps (shear stress 0.16 dyn/cm^2). (b) Bead-wall distance and (c) velocity histograms of all recorded time points for 8 beads (CD44- (grey) and CD44+ (red)) analysed for a selected shear stress (0.32 dyn/cm^2) at 100 fps. Average bead-wall distance (d) and velocities (e) of CD44- beads (black) and CD44+ beads (red). n = 9-70 beads. Error bars represent standard errors of the mean.

a single CD44+ bead showed an overall reduced velocity of ~ 15 µm/s (closed red squares) and lower bead-wall distance of ~20 nm (open red circles). In addition, the trajectory displayed transient 'stop' and 'go' phases, with the 'stop' phases (close-to-zero velocity) displaying reduced bead-wall distance compared to the 'go' phases. Such phases, in terms of velocity, have been observed with conventional imaging modes [43]. Here, we show that RICM provides the means to study the transient interactions in terms of bead-wall distance as well. This is in agreement with the pioneering work of Robert et al [29], who have demonstrated with RICM the detection of interactions of surfaces bearing the intercellular adhesion molecule ICAM-1 and beads coated with anti-ICAM-1 even in the presence of a thick HA film on the surface.

The CD44-HA-mediated interactions observed here were emphasized by generation of histogram plots of the trajectories of various beads (Fig. 6b-c). At a given shear stress (here 0.32 dyn/cm^2), the bead-wall distances and velocities were lower for the population of CD44+ beads compared to CD44- beads, with little overlap. The broad distribution of velocities for interacting beads compared to CD44- beads most likely arises through a superposition of two effects: small heterogeneities in the CD44 coverage, over the surface of each single bead and between individual beads; and the stochastic nature of interactions involving few CD44-HA bonds. Furthermore, the average bead-wall distance and velocity of CD44+ beads were consistently reduced compared to CD44- beads over a physiological range of shear stresses (0-1 dyn/cm^2, Fig. 6d-e).

Taken together, this example of the detection of CD44-HA-mediated adhesion demonstrates that our biomimetic cells and surfaces provide tools for probing physiologically relevant interactions *in vitro*. Furthermore, this highlights RICM as a useful detection tool, with high throughput data processing (capable of processing bead trajectories over 1000s of frames with fast output) and similar *xy* sensitivity to conventional imaging modes, but with the added opportunity to examine distances between the interacting bead and surface. Thus, our platform could be extrapolated to the further study of thick glycocalyx mimetics with diverse cell receptors that are required for various stages of the cell adhesion cascade, to help ascertain the role of the soft glycocalyx as a repulsive cushion modulating adhesion to endothelial cell surface receptors [29].

2.2.3. Visualising the contact area and rolling, and the formation of tethers and slings, of CD44+ T-lymphocytes

Our assay system can also be integrated with living cells. To illustrate this, living AKR1 T-lymphocytes, transfected with CD44, were injected into the flow channel bearing a HA840-h brush. Videos were taken simultaneously in RICM and bright-field microscopy as the cells interacted with the HA surface under flow. In order to capture the cells in RICM, the bottom-most surface of the cell was selected as the point of focus. In comparison to bright-field microscopy, in which the whole cell is visible, RICM is most sensitive to the part of the cell that is in direct contact with the surface.

In bright-field microscopy, the cells were observed to roll as they translocated across the HA surface under flow (Fig. 7a, Supplementary Videos 1-2). The rolling is evidenced in the snapshots shown in Fig. 7a by observation of a region-of-interest (identified by green arrow heads), whose position remains relatively stable despite substantial translocation of the cell in the direction of flow (Fig. 7a, bright-field, 30.5-32.3 s). The rolling was not uniform over time and in some occasions sliding motion could also be observed. Interestingly, as the cells interacted with the HA surface, protrusions could be observed both in front of and behind the cell, which were particularly evident at shear stresses >1 dyn/cm^2 (depicted by blue and white arrows, respectively, Fig. 7a-b). The observation of these structures in bright-field (with the focal plane at the bottom surface of the cell due to simultaneous RICM/bright-field imaging) suggests that they lie relatively close to the HA840 surface. Indeed, some protrusions were sufficiently close (up to a few μm) to the HA surface to be clearly observed in RICM as well (Fig. 7b, Supplementary Video 2). Similar structures have previously been observed at high shear stress for other cell types *in vitro* (e.g., via total internal reflection fluorescence microscopy), and *in vivo* (via intravital microscopy) [44, 45]. They are described as tethers, which anchor behind the cell and upon detachment project to the front of the cell thus becoming slings. Such tethers/slings have been implicated as important for immune cell trafficking, but so far have only been reported in a few instances. Indeed, their observation here is to our knowledge novel for this cell type, and may be seen in our assay due to the plane of focus being set at the bottom-most surface of the rolling cell. In conventional flow assays the focal position likely usually lies at the cell equator, that is, at a level where the cells are in focus but tethers/slings may not be easily observed. As such, tethers/slings may be more common than previously thought, and observable in detail with the methods stated here without the need of labelling techniques.

The simultaneous acquisition of images in bright-field and RICM provides diverse information about the cell's architecture as it rolls. Image analysis routines (implemented in ImageJ) provided the means to ascertain cell velocity, area and roundness, calculated as $4/\pi \times \text{Area}/(\text{Major axis})^2$, from bright-field images, and contact area size and roundness from RICM images, as demonstrated for a single cell
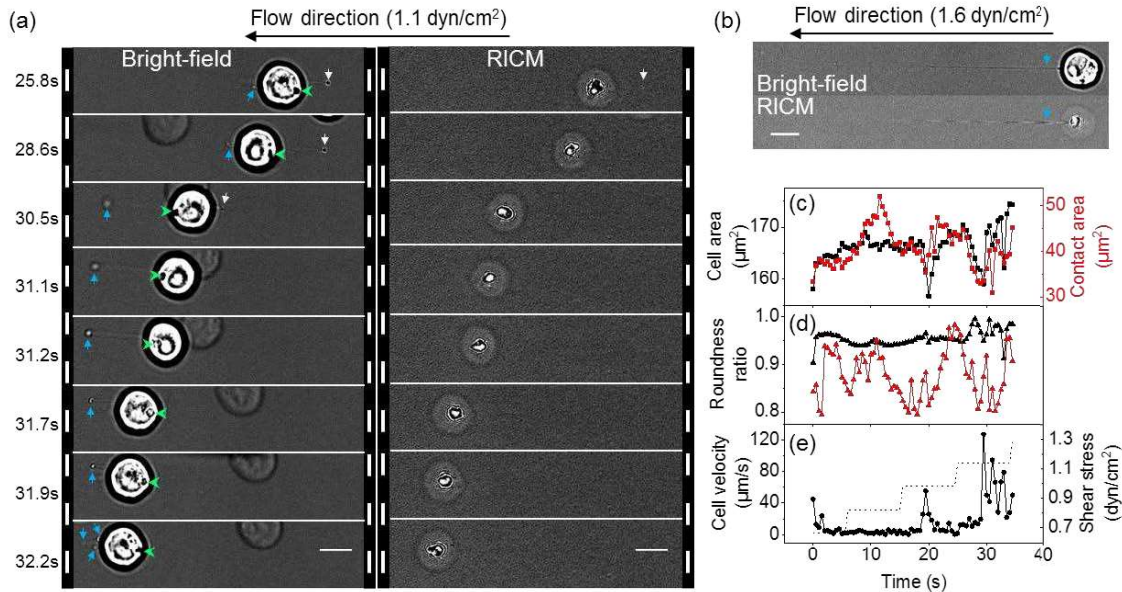
Fig. 7: Simultaneous bright-field and RIC microscopy of CD44+ T-lymphocytes on a HA840-h brush. (a) Images in bright-field (left) and RICM (right) as a cell rolled on the surface, under an imposed shear stress of 1.1 dyn/cm^2; a series of snapshots at selected times (indicated) is shown. Green arrows demonstrate a region-of-interest on the cell, whose movement demonstrates cell rolling. White and blue arrows point to tethers and slings, respectively. The bright-field image also shows a weaker 'ghost' image of the cell due to parasite reflections. (b) At an imposed shear stress of 1.6 dyn/cm^2, another cell has a long sling, observable in both bright-field and RICM. After the cell in (a) landed, the full trajectory was analysed as it rolled to determine the cell's projected area (from bright-field; c, black squares), contact area (from RICM, c, red squares), the roundness of the projected area (from bright-field; d, black triangles) and roundness of contact area (from RICM; d, red triangles), and velocity (from bright-field; e, black circles) under increasing shear stress (e, dashed line). Scale bar is 10 μm.

under flow (Fig. 7a, Supplementary Video 1). As well as highlighting the fluctuating cell shape and contact area shape as the cell rolled, these data also highlight the much smaller area of contact between the cell and HA surface compared to the overall cell size (Fig. 7c). Furthermore, while the overall cell showed a relatively round shape (Fig. 7d, black), the contact interface was less regular in shape (Fig. 7d, red), suggesting greater changes to the deformation of the contact area rather than the whole cell shape as the cell rolled. Further insight was obtainable by observation of cell velocity. For instance, during spikes in cell velocity (Fig. 7e, t = 20 s and 30 s, which coincided with tether detachment (Fig. 7a, Supplementary Video 1), cell area and contact area transiently decreased. Such observations suggest transient decompression of the flattened cell as it rolled faster, or heterogeneities in cell shape along its circumference, which were emphasized as it rolled.

The above analysis demonstrates how simultaneous imaging in bright-field and RICM reveals complementary insight regarding the dynamics of cell rolling, size, contact area and deformation as cells interact with a surface under flow. In addition, this example illustrates how biomimetic surfaces can be interfaced with living cells. This approach has the potential to be extended further, to observe circulating cell-mimetic beads on real glycocalyces on cultured endothelial monolayers [46], and even to live circulating cells on real glycocalyces. In this way, our integrated assay can encompass a large range of complexity, from fully reconstituted models that are well-defined and capture selected aspects of the cell-glycocalyx interaction in their pure form (thus facilitating mechanistic studies and the identification of new phenomena), to fully cellular systems that reproduce the complexity of the real endothelial glycocalyx-blood cell interactions more closely (thus facilitating tests of biological relevance).

3. Conclusion

The assay system reported here represents a new, integrated methodology to shed light on cell-

glycocalyx interactions under flow in mechanically and biochemically well-defined environments. The ability to track cells or cell-mimetics interactions with well-defined glycocalyx-mimetics in 3D offers the opportunity to study the importance of physical parameters of the endothelial glycocalyx. Here, we have reported on the development of model HA surfaces with tuneable physical and chemical properties and demonstrated the wealth of insight that they can provide on cell adhesion under flow with two selected examples. Such factors are inherent to physiological glycocalyces, and are likely to be modulated during inflammation. Therefore, this insight could be crucial to our understanding of how changes in inflammation can govern controlled cell entry to the endothelium. This could in the future be tackled by further exploitation of the proposed assay, and by comparison of cell adhesion behaviours across different HA brushes. Furthermore, while we have utilised HA-CD44-mediated cell-glycocalyx interactions to demonstrate our methodology here, this platform also provides room for diversity in glycocalyx-mimetics, allowing for co-presentation of glycocalyx components in various concentrations, combinations and architectures to untangle how biochemical and mechanical cues synergistically control the selective adhesion and migration of cells at the blood vessel wall.

4. Materials and methods

4.1. Materials

Experiments with cell- and surface-biomimetics were performed with HEPES buffer, pH 7.4: 10 mM HEPES (Fisher Scientific, Illkirch, France), 150 mM NaCl (Sigma Aldrich, Saint-Quentin Fallavier, France), 2 mM CaCl$_2$ (Sigma Aldrich) and 1 mM NaN$_3$.

Unfunctionalised and SuperAvidin (SuAv)-functionalised polystyrene microbeads were purchased from Polysciences Europe GmbH (Hirschberg, Germany). For CD44+ cell-mimetics, a recombinant protein containing the human extracellular domain of CD44 (residues 1-267) and a C-terminal biotin tag (bCD44) was generated as described previously [47]. The monoclonal anti-CD44 antibody IM7 conjugated to FITC (IM7-FITC) was purchased from Ozyme (Saint Quentin Yvelines Cedex, France).

For preparation of HA films as glycocalyx-mimetics, circular glass coverslips of 35 mm diameter (Fisher Scientific) were cleaned and coated with a 5 nm layer of gold [30], to yield a surface that remains transparent (for optical microscopy) yet displays the chemical properties of gold (required for thiol-monolayer formation). The gold-coating was performed using a mask to ensure that only the central part of the surface was coated with gold, while the outer parts were retained bare to guarantee an optimal seal of the laminar flow chamber. Oligo-ethylene glycol (OEG) thiol and biotinylated OEG (bOEG) thiol were purchased from Polypure, Oslo, Norway. SAv was purchased from Sigma Aldrich. Reducing-end biotinylated HA (bHA) with molecular weights 840 ± 60 kDa and 58 ± 3 kDa, prepared by in vitro chemo-enzymatic synthesis [48], were purchased from Hyalose, OK, USA. The automated solid-phase synthesis of the HAdp15 oligosaccharide, and conjugation with biotin at the reducing end, has been described in [34].

4.2. Methods

4.2.1. CD44+ bead functionalisation and characterisation

SuAv-beads were washed in HEPES buffer by centrifugation at 12000 × g for 5 min. Functionalisation with bCD44 was performed at a working volume of 50 µL and bead concentration of 0.5 % (w/v) for 1 hour at 22 °C with agitation in a thermomixer (Eppendorf) at 1000 rpm. CD44+ beads were then washed, as described above. Beads were stored at 4 °C, and used for flow assays within one week.

For flow cytometry, CD44+ beads were incubated with IM7-FITC for 1 h at 1400 rpm in a thermomixer (Eppendorf) in the dark. Beads were washed 5 times and 10000 events analysed with a BD LSR II Analyzer Flow Cytometer with DIVA 6.3.1 software (BD Biosciences). Error bars of flow cytometry data represent robust standard deviation: rSD = Median of $\{|X_i - Median_x|\}$ × 1.4826. The value 1.4826 adjusts the robust value to the equivalent of a normal population distribution. rSD values were calculated in BD FACSDiva Software.

4.2.2. Surface preparation ex situ

Gold-coated coverslips were exposed to UV/ozone (Jelight, Irvine, CA, USA) for 10 min and submerged in a thiol mixture composed of bOEG and OEG in a 2:98 molar ratio at a final thiol concentration of 1 mM in ethanol within a glass container. The submerged coverslip was stored at 4 °C for a minimum of 18 h and maximum of 1 week before use. Just prior to

assembly in the parallel-plate flow chamber, the coverslip was washed with ethanol and dried under N_2.

4.2.3. Functionalisation of HA films in situ within parallel-plate flow chamber

The circular parallel-plate flow chamber (GlycoTech, MD, USA) was fitted with inlet/outlet tubing (PTFE, with internal diameter 0.56 mm, Fisher Scientific) and a rubber gasket (spacer, with defined channel of dimensions: $0.250 \times 2.5 \times 20$ mm ($h \times w \times l$)). Prior to formation of HA brushes, the chamber was assembled with a blank 35 mm coverslip, held together under vacuum, and passivated with bovine serum albumin (BSA), as detailed below. To account for the dead volume of ~50 µL, passivation and functionalisation steps were preceded by injection at 100 µL/min for 1 min. Flow rates were controlled by a syringe-pump (KDS Legato 110).

BSA passivation was performed with 10 mg/mL BSA in HEPES buffer for 15 minutes at 20 µL/min plus 10 min without flow. This was followed by washing in ultrapure water for 25 min and drying the system by withdrawing air.

The gold-coated coverslip functionalised *ex situ* with bOEG/OEG (see above) was incorporated into the BSA-passivated flow chamber, and sealed under vacuum. The surface was washed with HEPES buffer at 50 µL/min for 10 min before functionalisation. Functionalisation steps were performed at a wall-shear stress of 0.0025 dyn/cm^2 (equal to a flow rate of 3.9 µL/min, Eq. (3)), in order to maintain the same wall shear stress (and thus the same mass transport conditions) as used in QCM-D experiments, which have previously been used to develop and characterise the surface functionalisation strategy [30, 31]. SAv was injected at a concentration of 20 µg/mL for 30 minutes, and the surface washed with HEPES buffer for 10 min. For HA films used in Fig. 4, addition of bHA was performed as follows: HAdp15, 1 µg/mL for 35 min; HA58, 1 µg/mL for 90 min; HA840-h, 20 µg/mL for 105 min; HA840-l, according to the sequential incubation steps shown in Fig. 3. The surfaces were washed in HEPES buffer for 10 min and left overnight to equilibrate in the absence of flow.

4.2.4. Cell culture

AKR1 T-lymphocytes, naturally CD44-, transfected with CD44+ were originally generated and kindly provided by Robert Hyman (SALK Institute, La Jolla, CA, USA). Cells were passaged twice a week and cultured in high glucose Dulbecco's modified eagle's medium (DMEM, Sigma Aldrich) supplemented with heat-inactivated fetal bovine serum (FBS) and penicillin (100 U/mL)/streptomycin (100 µg/mL) (Fisher Scientific) at 37 °C, 5 % CO_2 in T75 flasks (Fisher Scientific).

4.2.5. Multi-modal imaging and data acquisition

A commercial optical microscope was adapted to incorporate bright-field and RICM imaging modalities. We provide thorough details about this conversion, in Supplementary Information, Section S1.1, in order for other laboratories to follow this procedure should they desire.

For data acquisition of microbeads at rest and where lift was observed, RICM images were captured in two wavelengths. RICM videos were captured using an exposure time of 1.1 ms and frame rates as described in the main text.

For data acquisition with CD44+ AKR1 T-cells, dual bright-field and RICM images were captured with an exposure time of 30 ms and frame rate of 10 fps.

4.2.6. Flow assay with uncoated and CD44+ beads

Beads were injected onto HA films and left to settle for 5 min, and videos were then recorded in RICM under fixed flow rates. The flow rate, Q, was converted to shear stress, τ, by applying the following equation [39]:

$$\tau = \frac{6Q\eta}{h^2 w} \qquad \text{Eq. (4)}$$

with w and h the channel dimensions, and η the solution viscosity (~ 1 mPa.s at room temperature and 0.7 mPa.s at 37 °C). Measurements with microbeads were performed at a temperature of 24 °C. Tracking procedures of the beads in three dimensions are described in the Supplementary Information Section S1.8.

4.2.7. Flow assay with CD44+ cells

A HA840-h brush was formed at room temperature, on a monolayer of a modified-form of SAv, Traptavidin, which has slightly reduced dissociation kinetics for biotin for improved stability of HA brushes at 37 °C here [49]. The sample stage of the microscope was placed inside a box for control of temperature and set to 37 °C for flow assay experiments with cells. The working solution was exchanged for serum-free DMEM supplemented with 2.5 µg/mL of the antifungal agent Amphotericin B (Sigma Aldrich). Cells were injected on the HA840-h

surface under an imposed shear stress of 0.2 dyn/cm^2 and videos were recorded simultaneously in bright-field and RICM (60× oil objective). When cells were observed in the field of view a flow ramp was imposed, which covered a range of shear stresses from 0.2 to 5 dyn/cm^2.

Images were processed in ImageJ by performing a background subtraction (the background was generated by performing a z-project average intensity across the full video). Briefly, for analysis of cell velocity, area and roundness from bright-field images, cells were segregated from the background by applying a manually selected intensity threshold followed by conversion to a binary image. The resulting images were processed with Trackmate for velocity [50], and Analyse Particles for cell area and roundness. For analysis of contact area and roundness, RICM fringe patterns were manually segregated from the background and analysed with Analyse Particles.

5. Acknowledgements

6. References

1. Kolarova, H., Ambruzova, B., Svihalkova Sindlerova, L., Klinke, A., and Kubala, L., *Mediators Inflamm,* 2014: p. 694312.

2. O'Callaghan, R., Job, K.M., Dull, R.O., and Hlady, V., *Am J Physiol Lung Cell Mol Physiol,* 2011. **301**(3): p. L353-60.

3. Marsh, G. and Waugh, R.E., *J Vis Exp,* 2013(72): p. e50163.

4. Toole, B.P., *Semin Cell Dev Biol,* 2001. **12**(2): p. 79-87.

5. Nandi, A., Estess, P., and Siegelman, M.H., *J Biol Chem,* 2000. **275**(20): p. 14939-48.

6. Tammi, R., MacCallum, D., Hascall, V.C., Pienimaki, J.P., Hyttinen, M., and Tammi, M., *J Biol Chem,* 1998. **273**(44): p. 28878-88.

7. Wolny, P.M., Banerji, S., Gounou, C., Brisson, A.R., Day, A.J., Jackson, D.G., and Richter, R.P., *J Biol Chem,* 2010. **285**(39): p. 30170-30180.

8. Weinbaum, S., Tarbell, J.M., and Damiano, E.R., *Annu Rev Biomed Eng,* 2007. **9**(1): p. 121-167.

9. DeGrendele, H.C., Estess, P., and Siegelman, M.H., *Science,* 1997. **278**(5338): p. 672-5.

10. McDonald, B., McAvoy, E.F., Lam, F., Gill, V., de la Motte, C., Savani, R.C., and Kubes, P., *J Exp Med,* 2008. **205**(4): p. 915-27.

11. Khan, A.I., Kerfoot, S.M., Heit, B., Liu, L., Andonegui, G., Ruffell, B., Johnson, P., and Kubes, P., *J Immunol,* 2004. **173**(12): p. 7594-601.

12. Lesley, J., Schulte, R., and Hyman, R., *Exp Cell Res,* 1990. **187**(2): p. 224-33.

13. DeGrendele, H.C., Estess, P., Picker, L.J., and Siegelman, M.H., *J Exp Med,* 1996. **183**(3): p. 1119-30.

14. Clark, R.A., Alon, R., and Springer, T.A., *J Cell Biol,* 1996. **134**(4): p. 1075-87.

15. Christophis, C., Taubert, I., Meseck, G.R., Schubert, M., Grunze, M., Ho, A.D., and Rosenhahn, A., *Biophys J,* 2011. **101**(3): p. 585-93.

16. Hanke, M., Hoffmann, I., Christophis, C., Schubert, M., Hoang, V.T., Zepeda-Moreno, A., Baran, N., Eckstein, V., Wuchter, P., Rosenhahn, A., and Ho, A.D., *Biomaterials,* 2014. **35**(5): p. 1411-9.

17. Legras, S., Levesque, J.P., Charrad, R., Morimoto, K., Le Bousse, C., Clay, D., Jasmin, C., and Smadja-Joffe, F., *Blood,* 1997. **89**(6): p. 1905-14.

18. Hanke-Roos, M., Fuchs, K., Maleschlijski, S., Sleeman, J., Orian-Rousseau, V., and Rosenhahn, A., *Cell Adh Migr,* 2017. **11**(5-6): p. 476-487.

19. Richter, U., Wicklein, D., Geleff, S., and Schumacher, U., *Histochem Cell Biol,* 2012. **137**(5): p. 687-95.

20. Estess, P., DeGrendele, H.C., Pascual, V., and Siegelman, M.H., *J Clin Invest,* 1998. **102**(6): p. 1173-82.

21. Gal, I., Lesley, J., Ko, W., Gonda, A., Stoop, R., Hyman, R., and Mikecz, K., *J Biol Chem,* 2003. **278**(13): p. 11150-8.

22. DeGrendele, H.C., Kosfiszer, M., Estess, P., and Siegelman, M.H., *J Immunol,* 1997. **159**(6): p. 2549-53.

23. Zhuo, L., Kanamori, A., Kannagi, R., Itano, N., Wu, J., Hamaguchi, M., Ishiguro, N., and Kimata, K., *J Biol Chem,* 2006. **281**(29): p. 20303-14.

24. Mohamadzadeh, M., DeGrendele, H., Arizpe, H., Estess, P., and Siegelman, M., *J Clin Invest,* 1998. **101**(1): p. 97-108.

25. Lesley, J., Gál, I., Mahoney, D.J., Cordell, M.R., Rugg, M.S., Hyman, R., Day, A.J., and Mikecz, K., *J Biol Chem,* 2004. **279**(24): p. 25745-54.

26. Day, A.J. and de la Motte, C.A., *Trends in Immunology,* 2005. **26**(12): p. 637-643.

27. Paszek, M.J., DuFort, C.C., Rossier, O., Bainer, R., Mouw, J.K., Godula, K., Hudak, J.E., Lakins, J.N., Wijekoon, A.C., Cassereau, L., Rubashkin, M.G., Magbanua, M.J., Thorn, K.S., Davidson, M.W., Rugo, H.S., Park, J.W., Hammer, D.A., Giannone, G., Bertozzi, C.R., and Weaver, V.M., *Nature,* 2014. **511**(7509): p. 319-25.

28. Eyckmans, J., Boudou, T., Yu, X., and Chen, C.S., *Dev Cell,* 2011. **21**(1): p. 35-47.

29. Robert, P., Sengupta, K., Puech, P.H., Bongrand, P., and Limozin, L., *Biophys J,* 2008. **95**(8): p. 3999-4012.

30. Migliorini, E., Thakar, D., Sadir, R., Pleiner, T., Baleux, F., Lortat-Jacob, H., Coche-Guerente, L., and Richter, R.P., *Biomaterials,* 2014. **35**(32): p. 8903-15.

31. Baranova, N.S., Nilebäck, E., Haller, F.M., Briggs, D.C., Svedhem, S., Day, A.J., and Richter, R.P., *J Biol Chem,* 2011. **286**(29): p. 25675-86.

32. Thakar, D., Dalonneau, F., Migliorini, E., Lortat-Jacob, H., Boturyn, D., Albiges-Rizo, C., Coche-Guerente, L., Picart, C., and Richter, R.P., *Biomaterials,* 2017. **123**: p. 24-38.

33. Limozin, L. and Sengupta, K., *Chemphyschem,* 2009. **10**(16): p. 2752-68.

34. Dubacheva, G.V., Araya-Callis, C., Geert Volbeda, A., Fairhead, M., Codee, J., Howarth, M., and Richter, R.P., *J Am Chem Soc,* 2017. **139**(11): p. 4157-4167.

35. Attili, S., Borisov, O.V., and Richter, R.P., *Biomacromolecules,* 2012. **13**(5): p. 1466-77.

36. Lesley, J., Hascall, V.C., Tammi, M., and Hyman, R., *J Biol Chem,* 2000. **275**(35): p. 26967-75.

37. Banerji, S., Wright, A.J., Noble, M., Mahoney, D.J., Campbell, I.D., Day, A.J., and Jackson, D.G., *Nat Struct Mol Biol,* 2007. **14**(3): p. 234-9.

38. Frey, S., Richter, R.P., and Gorlich, D., *Science,* 2006. **314**(5800): p. 815-7.

39. Davies, H.S., Débarre, D., El Amri, N., Verdier, C., Richter, R.P., and Bureau, L., *Phys Rev Lett,* 2018. **120**(19): p. 198001.

40. Visintin, A., Mazzoni, A., Spitzer, J.H., Wyllie, D.H., Dower, S.K., and Segal, D.M., *J Immunol,* 2001. **166**(1): p. 249-55.

41. Alves, C.S., Burdick, M.M., Thomas, S.N., Pawar, P., and Konstantopoulos, K., *Am J Physiol Cell Physiol,* 2008. **294**(4): p. C907-16.

42. Freeman, S.A., Vega, A., Riedl, M., Collins, R.F., Ostrowski, P.P., Woods, E.C., Bertozzi, C.R., Tammi, M.I., Lidke, D.S., Johnson, P., Mayor, S., Jaqaman, K., and Grinstein, S., *Cell,* 2018. **172**(1-2): p. 305-317.e10.

43. Yago, T., Wu, J., Wey, C.D., Klopocki, A.G., Zhu, C., and McEver, R.P., *J Cell Biol,* 2004. **166**(6): p. 913-23.

44. Abadier, M., Pramod, A.B., McArdle, S., Marki, A., Fan, Z., Gutierrez, E., Groisman, A., and Ley, K., *Cell Rep,* 2017. **21**(13): p. 3885-3899.

45. Sundd, P., Gutierrez, E., Koltsova, E.K., Kuwano, Y., Fukuda, S., Pospieszalska, M.K., Groisman, A., and Ley, K., *Nature,* 2012. **488**(7411): p. 399-403.

46. Tsvirkun, D., Grichine, A., Duperray, A., Misbah, C., and Bureau, L., *Sci Rep,* 2017. **7**: p. 45036.

47. Bano, F., Banerji, S., Howarth, M., Jackson, D.G., and Richter, R.P., *Sci Rep,* 2016. **6**: p. 34176.

48. Jing, W., Michael Haller, F., Almond, A., and DeAngelis, P.L., *Analytical Biochemistry,* 2006. **355**(2): p. 183-188.

49. Chivers, C.E., Crozat, E., Chu, C., Moy, V.T., Sherratt, D.J., and Howarth, M., *Nat Methods,* 2010. **7**(5): p. 391-3.
50. Tinevez, J.Y., Perry, N., Schindelin, J., Hoopes, G.M., Reynolds, G.D., Laplantine, E., Bednarek, S.Y., Shorte, S.L., and Eliceiri, K.W., *Methods,* 2017. **115**: p. 80-90.

An integrated assay to probe endothelial glycocalyx-blood cell interactions under flow in mechanically and biochemically well-defined environments

Heather S. Davies,[1] Natalia S. Baranova,[2,‡] Nouha El Amri,[1] Liliane Coche-Guerente,[3] Claude Verdier,[1] Lionel Bureau,[1] Ralf P. Richter[2,4,*] and Delphine Débarre[1,*]

[1]Université Grenoble Alpes, CNRS, Laboratoire Interdisciplinaire de Physique (LIPhy), 38000 Grenoble, France. [2]Biosurface Lab, CIC biomaGUNE, Paseo Miramon 182, 20014 San Sebastian, Spain. [3]Université Grenoble Alpes, CNRS, Département de Chimie Moléculaire (DCM), Grenoble, France. [4]School of Biomedical Sciences, Faculty of Biological Sciences, School of Physics and Astronomy, Faculty of Mathematics and Physical Sciences, Astbury Centre for Structural Molecular Biology, University of Leeds, Leeds LS2 9JT, United Kingdom.

‡Current address: Institute of Science and Technology Austria (IST Austria), Am Campus 1, 3400 Klosterneuburg, Austria

*Corresponding authors: r.richter@leeds.ac.uk; delphine.debarre@univ-grenoble-alpes.fr

S1. Supplementary Information

S1.1 Reflection interference contrast microscope setup

This section provides all the necessary details to implement RICM on an existing inverted bright-field or epifluorescence microscope. In particular the RICM implementation described here does not require an anti-flex objective, commonly used in other setups, which extends its versality [1]. A simplified view of the microscope is shown in Fig. S1. A white light incoherent source (Light source: HPLS345, Thorlabs) was coupled into an inverted microscope (IX71, Olympus, Japan) using a custom-built illumination arm. Briefly, the light passed through a dichroic bandpass filter (BPF) to select the appropriate wavelength range for RICM. In the experiments presented in this paper, the filter was either a single-band green filter (for combined RICM/brightfield acquisitions; filter FF01-530/43-25, Semrock) or a dual-band green/red filter (for dual color RICM acquisitions; filter FF01-534/635-25, Semrock). For the photodamage assessment experiment, the filter was remove and the full spectrum of the lamp was used (covering the range 400-750 nm). The light then passed through an aperture diaphragm limiting the illumination angle on the sample. This graduated diaphragm (SM1D12C, Thorlabs) was imaged at the entrance pupil of the objective using two achromatic doublet lenses (AC254-100-A, Thorlabs). The graduations ensured that the maximum illumination angle used for different experiments was reproducible, and was set to an illumination numerical aperture (INA) of 0.46 [1].

The usual fluorescence cube in the microscope turret was replaced by polarisation optics: the light passed through a first polariser (WP25M-VIS, Thorlabs), was reflected by a polarising beamsplitter cube (PBS251, Thorlabs) and then passed through an achromatic, 15 mm-diameter imaging-flat quarter waveplate (QWP; custom-made, Fichou, France) before being focussed on the sample by an oil-immersion objective (60XO UPLSApo, Olympus, Japan). The beamsplitter cube was tilted by about 3° with respect to the optical axes to eliminate residual reflections from its faces. The axes of the quarter waveplate were positioned at 45° with respect to those of the polarizing cube, resulting in a circular polarization on the sample. Upon reflection on the sample, the circular polarisation was inverted, and converted again into a linear polarisation upon a second pass through the QWP. However, this linear polarisation is orthogonal to the incoming one so that the beam passes through the polarizing beamsplitter cube towards the imaging port of the camera.

For dual-colour imaging at high speed, a home-built image-splitting setup was used to simultaneously acquire a red and a green image on the camera: a variable slit at the imaging port of the microscope (VA100/M, Thorlabs) was used to limit the field of view to half of the height of the camera sensor. The image plane at the camera port of the microscope was then imaged onto the sCMOS camera (ORCA Flash 4.0 V2, Hamamatsu) using achromatic relay lenses (ITL200, Thorlabs). In between the two lenses, the green and red images were separated using an imaging-flat dichroic mirror (FF560-

FDi01-25x36, Semrock) gently held through curable silicon paste (Sugru, FormFormForm, UK) to avoid any image distortion. Silver mirrors (PFSQ10-03-P01, Thorlabs) were used to orient the two images onto different regions of the camera for simultaneous imaging of red and green signals. These two images were then spectrally cleaned by dichroic filters to avoid any crosstalk between the two signals (green: FF01-531/46-25; red: FF01-629/56-25, Semrock) and recombined with another identical dichroic mirror (FF560-FDi01-25x36, Semrock). In Fig. S1, an example of combined RICM (green)/ bright-field (red) imaging is shown. For bright-field imaging, a red coloured glass filter (FGL610S, Thorlabs) was used to filter the light for the microscope illumination arm that was subsequently focussed by a long-distance 0.3 NA condenser (all Olympus, Japan). An autofocus device (CRISP system, ASI imaging, USA) was mounted on the camera port of the microscope just before the variable slit to ensure that the focus was stable throughout our experiments. Finally, a custom-built thermostated box (Digital Pixel, UK) enclosing most of the microscope was used to control the temperature at the sample.

Further details on our experimental setup and analysis regimes are available upon request. In sections S1.2, S1.7 and S1.8 we also provide details of the implementation of RICM image analysis and resulting tracking precision.
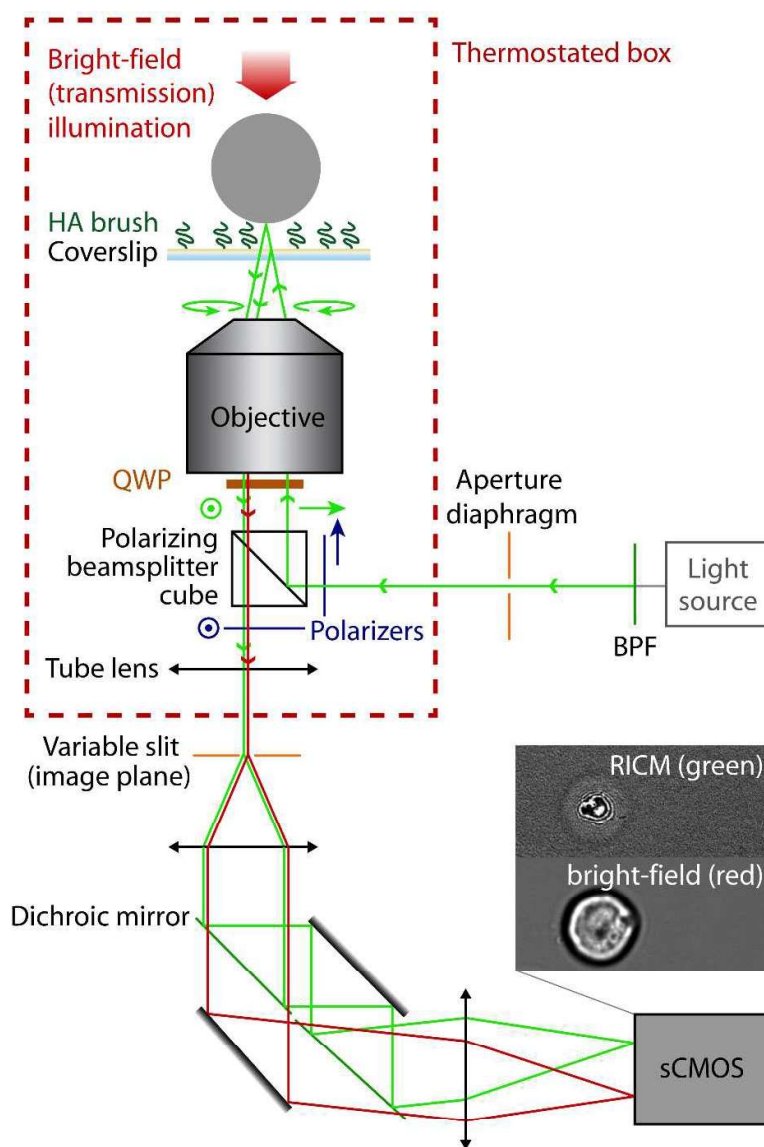

Figure S1: Schematic view of the multi-modal microscope used for imaging beads and cells.

S1.2 RICM pattern on bead as a function of bead height

RICM images are formed by the interference between light reflected from the substrate and from the polystyrene bead (Fig. S2). Multiple reflections inside the gold layer give rise to effective reflection coefficients r_1 and r_2, which are complex quantities. Around the bead centre ($r = 0$), the pattern is radially symmetric and its intensity as a function of the distance r from the centre can be written as:

$$I(r) = A_1 e^{-\frac{r^2}{w_1^2}} + A_2 e^{-\frac{r^2}{w_2^2}} \cos\left(\phi_0 + \frac{2\pi\, n_{\text{buffer}}}{\lambda} \delta h(r)\right) \tag{S1}$$

where A_1 and A_2 account for the amplitude of the offset and of the fringes, respectively, and w_1 and w_2 for their empirical decrease with the bead distance to the surface [2]. n_{buffer} is the refractive index of the medium; the change in refractive index due to the presence of the HA film can be neglected due to its small amplitude. $\delta h(r)$ describes the geometrical path length difference between the ray reflecting on the bead and the one reflecting on the gold surface. At the point of this latter surface where the reflection occurs, and in the case of a bead of large radius (typically > 5µm), it can be well approximated as:

$$\delta h(r) \approx 2h(0) + \frac{r^2}{R} - \frac{3}{4}\frac{r^4}{R^3} \tag{S2}$$

where R is the bead radius. Finally, ϕ_0 accounts for the phase difference in r_1 and r_2. Because this offset is very sensitive to the exact thickness of the gold layer, it is determined experimentally by measuring the RICM pattern obtained in the absence of the HA brush (as shown in Fig. 2).

From Equation S1, it can be seen that the RICM pattern is identical for all measured heights (h_{meas}) separated by $\frac{\lambda}{2n_{\text{buffer}}} \approx 200$ nm and so in order to ascertain the correct height, measurements were made at two wavelengths (534 nm, green and 635 nm, red). This method provides unambiguous determination of heights up to $\lambda_1 \lambda_2 / [2n_{\text{buffer}}(\lambda_2 - \lambda_1)] \approx 1.2$ µm [3]. If further distances need to be measured, a third wavelength (e.g., in the 400-500nm range) could be added to extend this range to ≈ 2 µm.
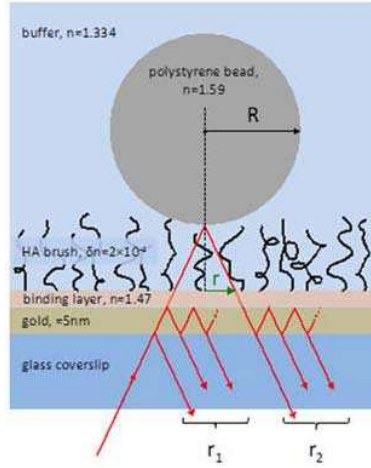

Figure S2: Sample structure and light reflection path. Multiple reflections occur in the gold layer, giving rise to two effective reflection coefficients, one before (r_1) and one after (r_2) reflection on the bead hovering over the functionalized surface. The value for the refractive index of the binding layer is indicative and not used in data analysis. A thin (~ 0.5 nm) titanium adhesion layer is present between the gold and the glass that is not shown in the figure, and its effects are, as for gold, incorporated in the phase offset ϕ_0. A value of 1.334 was used for the HEPES buffer for analysis both at $\lambda = 532$ and 635 nm (i.e. dispersion was neglected).

S1.3 Additional controls for thickness determination and stability of HA brushes

Key technical aspects related to the thickness determination and stability of HA brushes were corroborated further. We found that the size of microbeads had an appreciable effect on the bead-substrate distance (Fig. S3a), indicating that gravitational forces exerted by the beads can indent the HA brush. Importantly, this effect was negligible for bead diameters ≤ 25 μm and hence we used the 25 μm microbeads to determine HA brush thicknesses.

Secondly, validation of the illumination conditions used for image capture was performed by examination of the stability of another HA840 brush under various illumination settings. Under constant exposure of white, unfiltered light the thickness of the HA brush reduced significantly within just 1 h, demonstrating photo-damage to the surface (Fig. S3b, black bars). In contrast, under exposure of red/green filtered light (see Section S1.1), the HA brush thickness remained stable, demonstrating no photo-damage by illumination with the longer wavelengths of light (Fig. S3b, red bars).

These observations highlight that care should be taken to ensure that film thickness measurements are undertaken without film compression and that photo-damage should be assessed and limited by reducing the illumination intensity and using longer wavelengths. All subsequent measurements were thus performed with beads of diameter ≤ 25 μm imaged with either red or green light or combined red/green light.
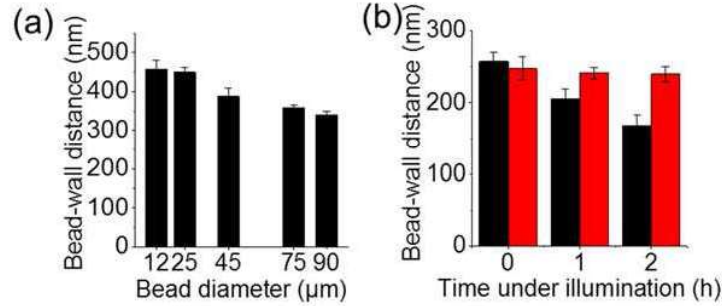

Figure S3: (a) Compression of another (more dense) HA brush by microbeads of higher diameter ($n \geq 27$). (b) Photo-damage of another (less dense) HA brush by constant exposure to white, unfiltered light (black) and red-green filtered light (red) ($n \geq 12$). Error bars show standard deviations.

S1.4 Estimating the elastic modulus of HA brushes from their grafting density

As discussed in detail in reference [4], contact mechanics and polymer brush theories can be combined in order to obtain the following expression for the elastic modulus of a brush:

$$M = \frac{kT}{\xi^3 (1 - h/H_0)^2 \pi} \left[7 \left(\frac{H_0}{h} \right)^{5/4} + 5 \left(\frac{h}{H_0} \right)^{7/4} - 12 \right] \quad (S3)$$

where kT is the thermal energy and h is the height of the compressed brush. Since the microbeads used here do not appreciably deform the brush (Fig. S3a), h/H_0 tends to one. In this limit of vanishing deformation, Eq. S3 tends to a finite value corresponding to the low strain elastic modulus, $M \approx 13$ $kT/(\pi \xi^3)$, as provided in the main text (Eq. 3).

S1.5 Estimating the elastic modulus of a soft film from indentation by bead gravitational force

The modulus derived from the rms distance (Eq. 3) can be compared to that obtained from data such as those provided in Fig. S3a, showing how the use of larger (hence heavier) microbeads results into compression of the HA840-h brush. As detailed in [4], the relationship between the compression of the brush and F_G, the gravitational force acting on the brush due to the bead's weight, reads:

$$F_G = \frac{4}{3}\pi R^3 g \Delta \rho = \frac{\pi M (H_0 - h)^2 R}{H_0} \qquad (S4)$$

with $g = 9.81$ m s^{-2}, $\Delta\rho$ the density difference between the bead and fluid (40 kg m^{-3} for polystyrene vs. water), and R the bead radius.

In Fig. S4, we replot the data of Fig. S3a as F_G as a function of $\pi R(H_0-h)^2/H_0$. It can be seen that the data indeed fall on a straight line, the slope of which yields the modulus M. From such an analysis, we compute $M = 35 \pm 5$ Pa, in good agreement with the value of 40 ± 18 Pa obtained from Eq. S3 and reported in the main text for the HA840-h sample.

Such a consistency check validates our use of Eq. S3 to estimate elastic moduli. It also shows that measuring the height of beads of various sizes is an easy means to probe the elastic response of a soft layer. While nominally simpler, and requiring no a priori knowledge of the molecular architecture of the layer, such a method is nonetheless limited to layers displaying moduli lower than about 1 kPa, above which the compression levels obtained with polystyrene microbeads would fall below the experimental accuracy of RICM. The use of denser (e.g., glass) microbeads would however allow probing layers of moduli up to 10 kPa.
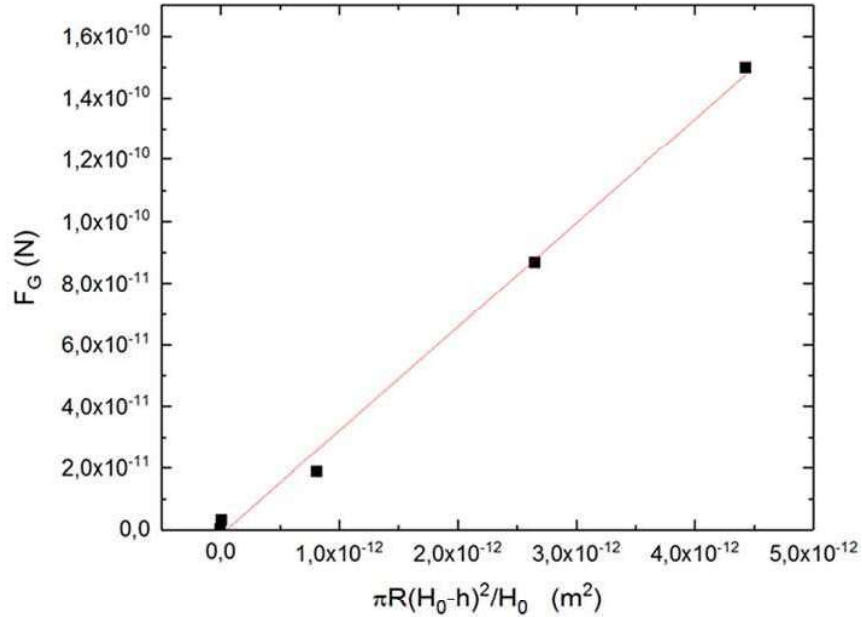

Figure S4. Plot of the compression data from Fig. S3a as F_G vs $\pi R(H_0-h)^2/H_0$ (symbols). The red line is a linear fit to the data, yielding a slope $M = 35 \pm 5$ Pa.

S1.6 Estimating the elastic modulus of a soft film from microbead lift under flow

We here propose an alternative method to estimate the elastic modulus that also does not require any prior knowledge of the film surface density and architecture and is based on the measurement of elastohydrodynamic lift. This lift arises from the flow-induced deformation of soft films by flowing (and non-interacting) microbeads, with the magnitude of lift correlating with film softness, as demonstrated for HA brushes in Fig. S5.

A quantitative analysis of elastohydrodynamic lift on HA brushes has been described in some detail in our recent work [4], and is adapted here in order to determine the brush elastic modulus, M, from measured lift and imposed shear stress. Neglecting inertial effects, which remain small in laminar flow assays, the vertical forces acting on a flowing bead are (i) the gravitational force (F_G) and (ii) the elastohydrodynamic force (F_{EHD}) arising from the glycocalyx deformation. The balance of these two opposing forces reads:

$$\underbrace{\frac{\eta^2 R^2 (V - R\Omega)^2 H_0}{M\delta^3}}_{F_{\text{EHD}}} = \underbrace{\frac{4}{3}\pi R^3 g \Delta\rho}_{F_{\text{G}}} \tag{S5}$$

with η the viscosity, g, $\Delta\rho$ and R as defined above, V the translational bead velocity, Ω the bead angular velocity, and δ the measured lift. In the limit where $\delta/R \ll 1$, V and Ω can in turn be expressed as a function of δ and the imposed shear rate $\dot\gamma$ as [4]:

$$V = \frac{\dot\gamma R \left(1 - \frac{\delta}{R}\right)}{0.7625 - 0.2562 \ln\left(\frac{\delta}{R}\right)} = \dot\gamma R \times F\left(\frac{\delta}{R}\right) \tag{S6}$$

$$R\Omega = \frac{\dot\gamma R}{1.6167 - 0.4474 \ln\left(\frac{\delta}{R}\right)} = \dot\gamma R \times G\left(\frac{\delta}{R}\right) \tag{S7}$$

Combining Eqs. S5 to S7 yields for M:

$$M = \frac{3\eta^2 \dot\gamma^2 H_0}{4\pi R^2 g \Delta\rho} f\left(\frac{\delta}{R}\right) \tag{S8}$$

with the function $f(\delta/R) = (F-G)^2/(\delta/R)^3$, where functions F and G are defined in Eqs. S6 and S7, respectively. Furthermore, $f(\delta/R)$ can be approximated, with better than 6% accuracy for δ/R in the range from 10^{-4} to 0.3, by:

$$f\left(\frac{\delta}{R}\right) \approx 0.11 \left(\frac{\delta}{R}\right)^{-2.827} + 1.8 \left(\frac{\delta}{R}\right)^{-1.83} \tag{S9}$$

Substituting shear stress, $\tau = \eta\dot\gamma$, provides:

$$M \approx \frac{3\tau^2 H_0}{4\pi R^2 g \Delta\rho} \left[0.11 \left(\frac{\delta}{R}\right)^{-2.827} + 1.8 \left(\frac{\delta}{R}\right)^{-1.83} \right] \tag{S10}$$

Using the highest measured lift for each brush (Fig. S5), the elasticity values computed with Eq. S10 were 4 Pa (HA840-l), 40 Pa (HA840-h) and 11 kPa (HA58). These values agree rather well with the elasticities computed through Eq. 3 (Fig. 4d), validating the analysis of elastohydrodynamic lift as an alternative method to determine the elasticity of soft brushes with appreciable lift.
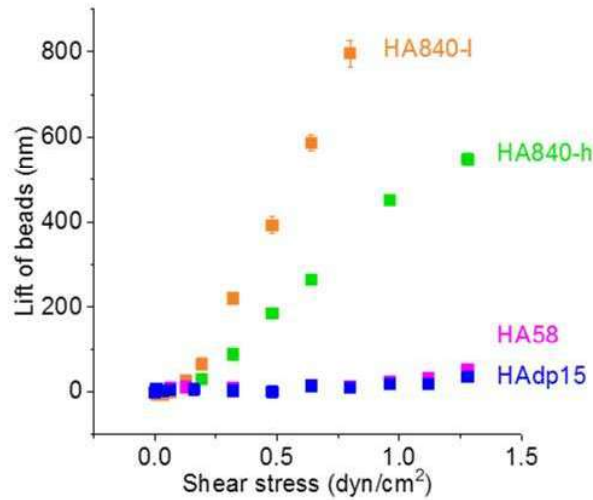

Figure S5. Lift (equal to the bead-wall distance after subtraction of the bead-wall distance at rest) on soft HA brushes (HAdp15 (blue), HA50 (magenta), HA840-h (green), HA840-l (orange)) measured by tracking the motion of uncoated microbeads in 3 dimensions with RICM under increasing wall shear stresses. Error bars show standard errors of the mean, which are typically smaller than the symbol size. For each shear stress ~20 beads were analysed. Data for polymer films taken from [4].

S1.7 CD44+ bead characterisation by flow cytometry

In order to estimate the density of CD44 on SuperAvidin (SuAv) beads, the biotin binding capacity of the beads was first established. SuAv coated 15 µm beads were functionalised with biotinylated-fluorescein (bFITC; M_W = 732.8; Thermofisher Scientific, France) and analysed by flow cytometry (Fig. S6a, red dataset). The bFITC saturation curve had a plateau at an intensity at I_{bFITC}^{sat} = 832 ± 242. The incubation concentration of bFITC required for saturation was 266 nM, which under the incubation conditions here (reaction volume of 50 µL and bead concentration of 0.5% (w/v)) gives a biotin binding capacity of 40 ng of bFITC per mg of beads. This value is in good agreement with the biotin-binding capacity of 16 ng/mg reported by the supplier; slight differences are likely due to experimental conditions, in which we examined a range of concentrations rather than an exact titration. From the provider's value for the biotin binding capacity, we compute a surface density at saturation of bFITC of $\rho_{bFITC}^{sat} \approx 32000$ molecules/µm².

Using the bFITC data as a reference for the density of sites available on the beads provides a comparison with bCD44 coated beads. As shown in Fig. S6a, the bCD44 fluorescence level was much lower than that of bFITC. This is despite the fact that IM7-FITC used to detect bCD44 has 3-7 FITC moieties compared to bFITC possessing just 1 fluorescein moiety, according to supplier information. We hypothesize that 15 µm beads show lower bCD44 coverage than b-fluorescein due to steric hindrance of larger bCD44 (~60 kDa) binding to SuAv compared to the very small bFITC (732.8 Da). To account for the difference in FITC stoichiometry, and to relate IM7-FITC fluorescence values to surface density of CD44, we normalise the raw level of fluorescence of IM7-FITC by dividing it by a factor of 5 (the average of 3 to 7 moieties per IM7-FITC molecule), to derive comparable data with bFITC. The surface density of CD44 (ρ_{bCD44}) is then computed from the normalised IM7-FITC fluorescence intensity ($I_{IM7\text{-}FITC}^{norm}$) as:

$$\rho_{bCD44} = \rho_{bFITC}^{sat} \frac{I_{IM7\text{-}FITC}^{norm}}{I_{bFITC}^{sat}} \qquad\qquad (S11)$$

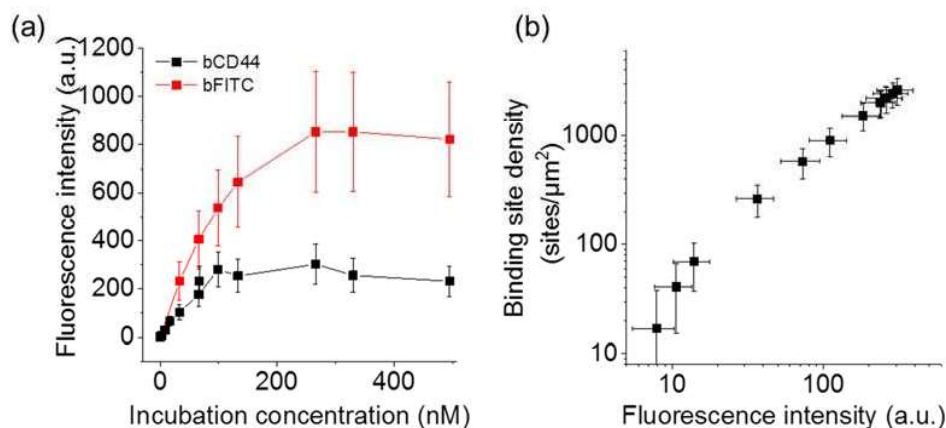This produced the data in Fig. S6b.

Figure S6: Characterisation of binding site density on CD44+ beads. (a) bFITC and bCD44 saturation curves of 15 µm SuAv beads. (b) Estimation of binding site density on CD44+ beads from fluorescence intensity. Error bars show rSD (normalised robust standard deviation from BD FACSDiva Software, *x* axis data) and calculated relative errors (*y* axis data). Data were measured on a LSRII flow cytometer with a FITC voltage of 400, and 10000 events per sample.

S1.8 3D tracking of beads with RICM

A schematic representation of the determination of the 3D trajectory of beads using RICM is shown in Fig. S7. First, the location of the bead centre was estimated in two dimensions using an iterative algorithm based on the symmetry of the RICM pattern: a window for pattern analysis was approximately centred around the bead, manually for the first time point of the sequence (red square in Fig. S7). This sub-image *Im1* was then flipped with respect to its centre, yielding image *Im2*, and the correlation of two resulting images was calculated. This calculation is performed as $FT^{-1}(FT(Im1) \times FT(Im2)^*)$, where $*$ denotes complex conjugation and TF is the Fourier Transform operation: using Fourier Transform operation ensures that the tracking can be achieved at high speed, hence allowing high-throughput analysis. The resulting cross-correlation image indicates, for all relative displacements of *Im1* and *Im2*, how well they are superimposed. It exhibits a peak that corresponds to their best superposition displaced from its centre by a distance [$2x,2y$] equal to twice the distance between the centre of the RICM pattern and that of the initial (red) window. x and y are then estimated with subpixel resolution by fitting the inter-correlation peak (parabolic fit on 5×5 points around the peak), which knowing the coordinates of the red window in the initial image provides the 2D coordinates of the bead in image n. For image $n + 1$, the window is centred around this estimated coordinate and the process is iterated, finally providing the in-plane trajectory of the bead. This method ensures that the bead can be tracked even if its RICM pattern changes due to a change in height, provided that the displacement between two images is smaller than half the size of the window. In the program the window size can be adjusted for the tracking of beads that cover a range of displacements between each frame.

For each time point, once the centre of the RICM pattern is determined, the pattern is azimuthally averaged to provide an experimental $I(r)$ curve (with r the distance from the bead centre) that is fitted using Equations S1 and S2. $h(0)$ is extracted from the difference in phase of the centre of the pattern (at $r = 0$) between the image of interest and a reference image at rest in the absence of an HA brush.
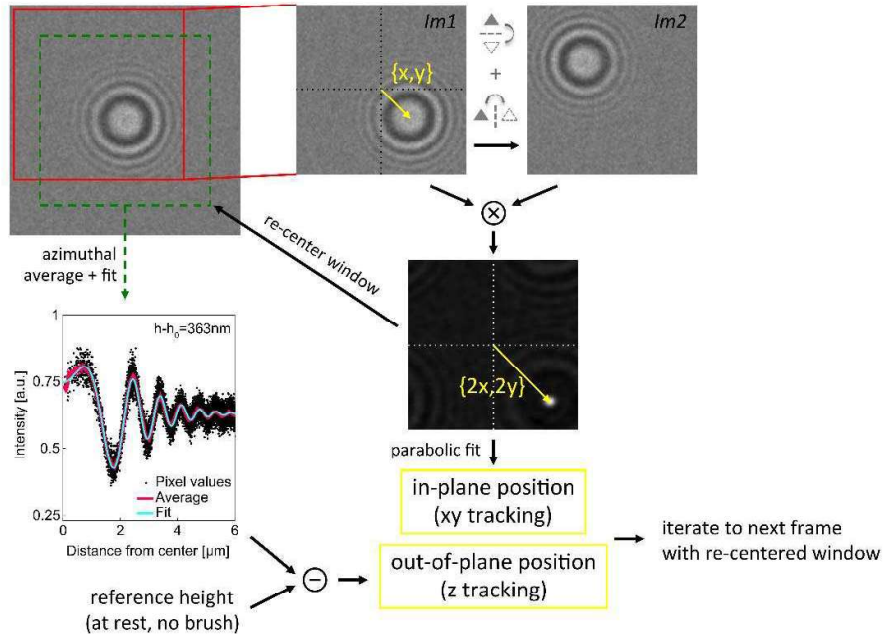

Figure S7: 3D tracking of beads in RICM images. This figure illustrates the procedure applied at each time point, which provides the in-plane position and subsequently the out-of-plane position of the bead. When iterating over the whole time sequence, one obtains the *xy*-trajectory with the former and the *z*-trajectory from the latter.

S1.9 Estimating the precision of in-plane tracking of beads

To estimate the precision of our tracking procedure in the xy plane, we recorded time sequences of non-interacting beads hovering above a SAv layer (5 beads) and a HA840-h brush (5 beads) in the absence of flow. The beads exhibit Brownian motion that can be characterized by plotting their mean square displacement (MSD), $<r(t + \tau) - r(t)>$ (where r denotes the in-plane displacement between times t and $t + \tau$, and $<>$ is the average over the whole trajectory, i.e. over t), as a function of the time interval τ (Fig. S8). In the absence of flow the resulting curve should be linear with a slope $4D$, where D is the diffusion coefficient of the sphere in the medium. Here, we measured $D \approx 3.7 \times 10^{-14}$ m^2.s^{-1}, slightly lower than the theoretical value (5.8×10^{-14} m^2.s^{-1}) as expected for a bead hovering close to a wall. Compared to the theoretical prediction of a linear curve, however, experimental data points when excluding $\tau = 0$ exhibit a constant offset, so that the data can be fitted instead by MSD(τ) = $\Delta r + 4 D \tau$, where Δr is the precision of the bead tracking with our algorithm. With this method, we find $\Delta r = 5.5 \pm 1$ nm rms, highlighting the good precision of our tracking procedure.

It can be noted also that the value of the diffusion coefficient can be used to estimate the fluctuations of velocity that are expected to be observed for 15 μm diameter beads tracked at 100 Hz: these fluctuations should have a standard deviation of the order of 2 to 3 μm.s^{-1}, which corresponds to experimental observations on non-interacting beads under flow (see Fig. 6a, black dots). This confirms that the fluctuations observed on bead trajectories under flow are due to Brownian motion or interactions with the substrate rather than to the precision limit of the tracking.
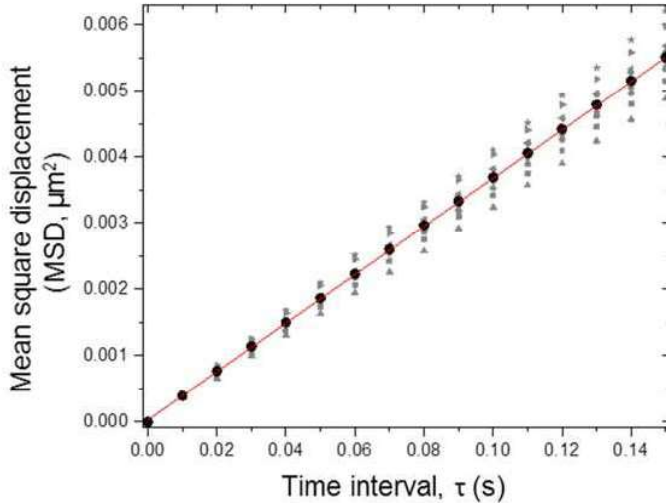

Figure S8: Estimation of the tracking precision in the xy plane from RICM images. 25 s trajectories were acquired at 100 Hz (2500 images) for 10 different 15-μm-diameter beads resting on a SAv layer (5 beads) or a HA840-h brush (5 beads). Gray symbols are MSDs of individual beads while the black dots are the ensemble average over the 10 beads. The red line is a linear fit excluding the data point at time interval $\tau = 0$, and does not pass through point (0,0) due to the precision error, which can be graphically evaluated as square root of the distance at $\tau = 0$ between the red line and the black dot.

S2. <u>Supplementary References</u>

1. Limozin, L. and Sengupta, K., *ChemPhysChem,* 2009. **10**(16): p. 2752-68.
2. Raedler, J. and Sackmann, E., *Langmuir,* 1992. **8**(3): p. 848-853.
3. Schilling, J., Sengupta, K., Goennenwein, S., Bausch, A.R., and Sackmann, E., *Phys Rev E Stat Nonlin Soft Matter Phys,* 2004. **69**(2 Pt 1): p. 021901.
4. Davies, H.S., Débarre, D., El Amri, N., Verdier, C., Richter, R.P., and Bureau, L., *Phys Rev Lett,* 2018. **120**(19): p. 198001.